The uppermost mantle seismic velocity structure of West Antarctica from Rayleigh wave tomography: insights into tectonic structure and geothermal heat flow

J. P. O'Donnell[1], G. W. Stuart[1], A. M. Brisbourne[2], K. Selway[3], Y. Yang[3], G. A. Nield[4], P. L. Whitehouse[4], A. A. Nyblade[5], D. A. Wiens[6], R. C. Aster[7], S. Anandakrishnan[5], A. D. Huerta[8], T. Wilson[9] and J. P. Winberry[8]

(July 15, 2019)

(1) School of Earth and Environment, The University of Leeds, Leeds, LS2 9JT, UK

(2) British Antarctic Survey, Natural Environment Research Council, Cambridge CB3 0ET, UK

(3) Department of Earth and Planetary Science, Macquarie University, North Ryde, NSW 2109, Australia

(4) Department of Geography, Durham University, South Road, Durham, DH1 3LE, UK

(5) Department of Geosciences, The Pennsylvania State University, University Park, PA 16802, USA

(6) Department of Earth and Planetary Sciences, Washington University, St. Louis, MO 63160, USA

(7) Department of Geosciences, Colorado State University, Fort Collins, CO 80523, USA

(8) Department of Geological Sciences, Central Washington University, Ellensburg, WA 98926, USA

(9) School of Earth Sciences, Ohio State University, Columbus, OH 43210, USA

* Corresponding author, j.p.odonnell@leeds.ac.uk

Abstract

Key words: Antarctica, seismology, tectonics, lithosphere, mantle, heat flow

We present a shear wave model of the West Antarctic upper mantle to ∼200 km depth with enhanced regional resolution from the 2016-2018 UK Antarctic Seismic Network. The model is constructed from the combination of fundamental mode Rayleigh wave phase velocities extracted from ambient noise (periods 8-25 s) and earthquake data by two-plane wave analysis (periods 20-143 s). We seek to (i) image and interpret structures against the tectonic evolution of West Antarctica, and (ii) extract information from the seismic model that can serve as boundary conditions in ice sheet and glacial isostatic adjustment modelling efforts. The distribution of low velocity anomalies in the uppermost mantle suggests that recent tectonism in the West Antarctic Rift System (WARS) is mainly concentrated beneath the rift margins and largely confined to the uppermost mantle (<180 km). On the northern margin of the WARS, a pronounced low velocity anomaly extends eastward from beneath the Marie Byrd Land dome toward Pine Island Bay, underlying Thwaites Glacier, but not Pine Island Glacier. If of plume-related thermal origin, the velocity contrast of ∼5% between this anomaly and the inner WARS translates to a temperature difference of ∼125-200 °C. However, the strike of the anomaly parallels the paleo-Pacific convergent margin of Gondwana, so it may reflect subduction-related melt and volatiles rather than anomalously elevated temperatures, or a combination thereof. Motivated by xenolith analyses, we speculate that high velocity zones imaged south of the Marie Byrd Land dome and in the eastern Ross Sea Embayment might reflect the compositional signature of ancient continental fragments. A pronounced low velocity anomaly underlying the southern Transantarctic Mountains (TAM) is consistent with a published lithospheric foundering hypothesis. Taken together with a magnetotelluric study advocating flexural support of the central TAM by thick, stable lithosphere,

this points to along-strike variation in the tectonic history of the TAM. A high velocity anomaly located in the southern Weddell Sea Rift System might reflect depleted mantle lithosphere following the extraction of voluminous melt related to Gondwana fragmentation. Lithospheric thickness estimates extracted from 1D shear wave velocity profiles representative of tectonic domains in West Antarctica indicate an average lithospheric thickness of ∼85 km for the WARS, Marie Byrd Land, and Thurston Island block. This increases to ∼96 km in the Ellsworth Mountains. A surface heat flow of ∼60 mW/m^2 and attendant geotherm best explains lithospheric mantle shear wave velocities in the central WARS and in the Thurston Island block adjacent to Pine Island Glacier; a ∼50 mW/m^2 geotherm best explains the velocities in the Ellsworth Mountains, and a ∼60 mW/m^2 geotherm best explains a less well-constrained velocity profile on the southern Antarctic Peninsula. We emphasise that these are regional average (many hundreds of km) heat flow estimates constrained by seismic data with limited sensitivity to upper crustal composition.

1 Introduction

West Antarctica owes much of its tectonic heritage to the Jurassic breakup of Gondwana and ensuing dispersal of microplate fragments (e.g., Dalziel & Elliot, 1982; Dalziel, 1992). The development of the West Antarctic Rift System (WARS), the uplift of the Transantarctic Mountains (TAM) and the impact of a putative mantle plume beneath Marie Byrd Land (MBL) have dominated the late Cretaceous to Paleogene evolution of West Antarctica (Figure 1) (e.g., LeMasurier & Landis, 1996; Fitzgerald, 2002). With geological exposures limited by the West Antarctic Ice Sheet (WAIS), delineation of tectonic domains and recent tectonism is reliant on geophysical probing. Owing to the deployment of broadband seismometer arrays, the seismic structure of much of the Antarctic crust and upper mantle is now reasonably well mapped (e.g., An et al., 2015b; Heeszel et al., 2016; Shen et al., 2018).

We construct a shear wave model based on fundamental mode Rayleigh wave phase velocities focussing on the uppermost mantle structure (<200 km) of West Antarctica. The model offers enhanced regional resolution through the inclusion of stations from the 2016-2018 UK Antarctic Seismic Network (UKANET, Figure 1). In the first half of this paper we describe the seismic data, processing and inversion, and interpret the structures imaged against the tectonic evolution of West Antarctica. In the second half we extract information that can be used to improve the accuracy of ice sheet and glacial isostatic adjustment (GIA) modelling efforts. Geothermal heat flow moderates ice sheet behaviour: it affects the viscosity of basal ice and, if sufficiently high, can generate lubricating meltwater that reduces friction with the bed (e.g., Martos et al., 2017). Pine Island Glacier and Thwaites Glacier in West Antarctica (Figure 1) are of particular concern because they are thought susceptible to marine ice sheet instability (e.g., Barletta et al., 2018). GIA is sensitive to lithospheric thickness and its lateral variation (e.g., Nield et al., 2018). From our shear wave model, we extract lithospheric

thicknesses and model the regional average geotherms and heat flows best describing 1D velocity profiles at representative tectonic locations in West Antarctica.

2 Tectonic Setting

East Antarctica was amalgamated from Archean nuclei in the Mesoproterozoic, eventually forming the core of Gondwana (e.g., Dalziel, 1992). The Mesozoic fragmentation of Gondwana was preceded by the emplacement of the Karoo-Ferrar large igneous province in East Antarctica and southern Africa at ∼185-177 Ma (e.g., Storey & Kyle, 1997; Fitzgerald, 2002, and references therein) and the development of the Weddell Sea Rift System (WSRS), a broad extensional/transtensional province within a distributed plate boundary between East and West Antarctica (e.g., Jordan et al., 2017). Karoo-Ferrar magmatism has been linked with a putative mantle plume in the proto-Weddell Sea region, potentially a driver for Gondwana breakup (e.g., Storey & Kyle, 1997).

West Antarctica is regarded as an assemblage of discrete crustal blocks separated by subglacial depressions. Three of the main four blocks - the Antarctic Peninsula, Thurston Island and Marie Byrd Land - are fore-arc and magmatic-arc terranes developed along the paleo-Pacific margin of Gondwana (e.g., Dalziel, 1992). The fourth block, the Haag-Ellsworth Whitmore (HEW) block, is regarded as an allochthonous continental fragment translated and rotated to its present location from an original pre-Gondwana-breakup position close to the East Antarctic plate and/or southern Africa. Exposed lithologies in the HEW block include a ∼13 km thick Paleozoic sedimentary sequence in the Ellsworth Whitmore Mountains, and Precambrian basement dated to ∼1 Ga in the Haag Nunataks (e.g., Storey & Kyle, 1997; Jordan et al., 2017, and references therein).

The tectonic regime in West Antarctica switched from compressional to extensional

following subduction of the Pacific-Phoenix spreading center at ∼110-105 Ma. The West Antarctic Rift System formed as MBL and Thurston Island moved away from the East Antarctica craton, with the major WARS extensional phase occurring between ∼105-85 Ma (e.g., Fitzgerald, 2002, and references therein). Paleogene extension was limited to the western Ross Sea and accompanied by rapid exhumation and uplift of the Transantarctic Mountains. In MBL an estimated maximum ∼3 km of tectonic uplift associated with alkaline volcanism beginning at ca. 28-30 Ma is cited as evidence of a mantle plume (e.g., LeMasurier & Landis, 1996). Others favour a model of subduction-related alkaline magma genesis in MBL (e.g., Finn et al., 2005). Inferred Neogene reactivation of subglacial troughs in central West Antarctica has been linked with Neogene extensional pulses in the western Ross Sea (e.g., Lloyd et al., 2015, and references therein).

3 Seismic Arrays

The International Polar Year 2007-2008 motivated the first deployment of year-round broadband seismometer arrays in the interior of Antarctica. As part of the POLENET-ANET project, a backbone array was deployed across Antarctica (Figure 1). The extant array comprises a mixture of cold-rated Güralp CMG-3T 120 s and Nanometrics Trillium 240 s seismometers sampling at 1 and 40 samples per second (sps).

Denser temporary arrays have intermittently supplemented the POLENET-ANET backbone array in West Antarctica, the most recent of which was the 2016-2018 UKANET array. This consisted of 10 cold-rated Güralp CMG-3T 120 s seismometers sampling at 1 and 100 sps (Figure 1 and Table S1). The 2015-2017 POLENET-ANET mini-array was complementary in design and location to the UKANET array.

Additional coverage is provided by the Antarctic Seismographic Argentinean Ital-

ian Network (ASAIN), station PMSA of the Global Seismographic Network (GSN) and the 1997-1999 Seismic Experiment in Patagonia and Antarctica network (SEPA) shown in Figure 1.

4 Two-Plane-Wave Tomography

Surface wave amplitudes and phases observed across seismic arrays often exhibit effects reminiscent of interference. This motivated Forysth & Li (2005) to model the wavefield as the superposition of two interfering plane waves. We applied this two-plane-wave method to fundamental mode Rayleigh waves recorded on the UKANET, POLENET-ANET, ASAIN and SEPA arrays and PMSA station over the periods 1997-1999 and 2010-2018. To garner good quality waveforms, we examined earthquakes with magnitudes $\geq$5.5 located within a distance of 120° of the composite seismic array. Earthquakes located within $\sim$30° of the array were excluded because the wave fronts cannot be considered planar at incidence.

An initial cull of earthquakes giving poor signal-to-noise ratio seismograms was carried out by visual inspection. Instrument responses were deconvolved from the remaining seismograms and these filtered into 12 $\times$ 10 mHz wide frequency bands with centre periods ranging from 20 to 143 s using a zero-phase-shift, four-pole Butterworth filter centred at the period of interest (Figure 2). Next, for each earthquake a window was manually defined at each period to isolate the fundamental mode Rayleigh waves from other seismic phases and/or interfering lateral refractions. At each period, only those earthquakes yielding high signal-to-noise ratio Rayleigh waves at at least five stations were considered for two-plane-wave tomography (2PWT). Out of a total of $\sim$2700 earthquakes screened, 457 were deemed suitable for analysis (Figure 2). Following Forysth & Li (2005), we assigned a prior data uncertainty of 10% to the phase and amplitude of each Rayleigh wave.

In the 2PWT inversion, at each period the Rayleigh wave phase velocity map best explaining phase and amplitude variations between stations was inferred on a grid with a node spacing of 100 km spanning West Antarctica. Being predicated on the assumption of planar wave fronts, the validity of 2PWT varies inversely with the areal extent of the seismic array. In response, we subdivided the expansive composite array into three sub-arrays approximately coincident with the Antarctic Peninsula, eastern West Antarctica and central West Antarctica. In this scheme, a given earthquake is effectively treated as three separate earthquakes, each incident on one of the sub-arrays. Following Yang & Forsyth (2006), finite frequency sensitivity kernels were used to represent the sensitivities of Rayleigh wave phases and amplitudes to structure. A smoothing length scale of 140 km gave the best compromise between unduly rough models arising from over-fitting data at the shortest length scales and under-fit models at the longest length scales (Figure S1). Using the 1D average phase velocity curve inferred by Heeszel et al. (2016) as a starting model, we initially inverted for a 1D average phase velocity curve representing our study area to serve as a starting model for the 2D tomographic inversions (Figure 3).

5 Rayleigh Wave Phase Velocities

Figure 4 shows the inferred 2D Rayleigh wave phase velocity uncertainty, calculated from the posterior model covariance matrix, at periods 25, 80 and 125 s. As expected, the uncertainty is least where the concentration of seismic stations is greatest and increases toward the grid periphery. Superimposed on the lateral variations is a trend of increasing uncertainty with increasing period, a reflection of the progressively increasing wavelength of the Rayleigh waves and hence decreasing resolution.

Figure 4 also shows the resolving capability of the inversion. The resolution matrix indicates that the morphology of velocity anomalies of length scale 400 km is recovered

with high fidelity within the polygon on Figure 4 at all periods. At periods 125 and 143 s there is some diminution in amplitudes at this length scale, but at all shorter periods amplitude recovery is generally better than 90%. Amplitude resolution at periods 125 and 143 s reaches this level for a length scale of 500 km.

The resolution matrix gives an overly optimistic picture of resolution at peripheral grid regions beyond the footprint of the seismic array. In subsequent plots we confine our discussion to the region enclosed by the polygon. Within this region (i) phase velocity uncertainty is generally less than ∼0.02-0.03 km/s at periods below 80 s and less than ∼0.05 km/s at periods 100-143 s, (ii) the resolution matrix indicates that velocity structure of length scale 400-500 km is imaged with high fidelity and (iii) imaged velocity structure transitions credibly between periods.

Figure 5 shows Rayleigh wave phase velocity maps at selected periods. At periods ∼20-30 s Rayleigh wave propagation is most sensitive to variations in crustal thickness: if the crust is thick, Rayleigh waves at these periods largely sample lower crustal rock, whereas if the crust is thin they largely sample seismically-faster mantle rock. At 25 s for example, relatively slower phase velocities coincident with the TAM, the HEW block, MBL, the southern Antarctic Peninsula and northern WSRS are consistent with thicker crust (e.g., Chaput et al., 2014; O'Donnell & Nyblade, 2014; Shen et al., 2018). In contrast, relatively faster phase velocities underlying the Ross and Amundsen Sea Embayments in the WARS and in the southern WSRS are likely the signature of mantle rock, and hence thinner crust.

At periods 40 s and above the Rayleigh wave phase velocities predominantly reflect uppermost mantle structure. The geological dichotomy of Antarctica is here apparent: slower phase velocities characterising the West Antarctic uppermost mantle contrast with faster velocities underlying East Antarctica. Prominent slow phase velocity anomalies at these periods occur beneath MBL and a portion of the southern TAM. Notably, the slow velocity anomaly underlying MBL extends eastward beyond

the MBL topographic dome toward Pine Island Bay. Offshore MBL a slow velocity anomaly coincides with the location of the Marie Byrd Seamounts and is conceivably the source thereof.

6 Shear Wave Velocities

At each grid node, a phase velocity dispersion curve (periods 20-143 s) was extracted by sampling the 2PWT phase velocity maps. These curves were merged with counterparts extracted from ambient noise tomography (ANT) Rayleigh wave phase velocity maps developed by the authors (O'Donnell et al., 2018). The shorter period ANT data (periods 8-25 s) have a greater sensitivity to crustal structure than the 2PWT data. Figure 6 compares ANT- and 2PWT-inferred phase velocity maps at 25 s and shows an example of a composite 8-143 s phase velocity dispersion curve obtained by weighted least squares polynomial regression of the ANT- and 2PWT-curves. Differences in processing, inversion and regularisation schemes result in minor disparity between ANT- and 2PWT-inferred velocities, but they generally agree within uncertainty bounds at overlapping periods. The areal extent of the ANT model domain, however, is less extensive than the 2PWT domain, so merged ANT-2PWT dispersion curves are restricted to the ANT domain. The phase velocity dispersion curves were subsequently inverted for 1D shear wave velocity structure. Because Rayleigh waves are most sensitive to vertically-polarised shear wave velocity, V_{SV}, we inferred V_{SV} rather than isotropic V_S.

The V_{SV} models were parameterised by ice and/or water layers overlying crustal and uppermost mantle layers. Ice thicknesses and water depths were taken from BEDMAP2 and allowed to vary within their uncertainty limits (Fretwell et al., 2013). The ice shear wave velocity was permitted to range between 1.82-2.02 km/s with a density fixed at 910 kg/m^3. We opted to not invert for a sedimentary layer because (1)

Rayleigh waves have limited sensitivity to shallow crustal structure in the period range considered and (2) sediment thickness estimates to guide the inversion are extremely limited. The 1D V_{SV} structure of the underlying crustal layer was parameterised using 4 cubic B-splines and a crustal thickness permitted to vary ±5 km from initial estimates extracted from the An et al. (2015b) Antarctic crustal model. The 1D uppermost mantle V_{SV} structure was parameterised using 5 cubic B-splines to a depth of 250 km, below which PREM V_{SV} values were adopted. In a Bayesian framework, we permitted crustal and uppermost mantle V_{SV} velocities to explore a broad ±20% range around initial PREM V_{SV} velocities, a range which encompasses published Antarctic velocity models (e.g., An et al., 2015b). This suite of constraints informed the prior model probability density function (PDF).

The likelihood function for dispersion curve prediction used the *Mineos* package (`https://geodynamics.org/cig/software/mineos/`). Crustal compressional wave velocities and densities were scaled from inferred shear wave velocities using regressions reported in Brocher (2005), while upper mantle counterparts were scaled using a Vp/Vs ratio of 1.74 and Birch's law (Birch, 1961). PREM Q values were used to correct for anelastic attenuation. A Markov chain Monte Carlo sampling scheme based on the Delayed Rejection Adaptive Metropolis algorithm built the posterior model PDF from the final 2,500 accepted models of 100,000 simulations (Guo et al., 2016, and references therein).

6.1 Tectonic Interpretation

Figure 7 shows a selection of 1D V_{SV} profiles representative of their parent tectonic domains in West Antarctica: station PIG3 lies adjacent to Pine Island Glacier in the Thurston Island block; station FOWL is close to the Haag Nunataks of the HEW block; node 1624 is in the Ellsworth Mountains of the HEW block; station BREN

is at Brenneke Nunatak on the southern Antarctic Peninsula; station SILY is at Mount Sidley in MBL; station BYRD is in the central WARS; station DUFK is at the Dufek Intrusion at the margin of the WSRS; and station SURP is at the southern TAM front (see Figure 1 and Table S1). The average standard deviation of inferred mantle V_{SV} velocities is generally less than ∼0.075 km/s, increasing to ∼0.1 km/s for locations (e.g., BREN) at the periphery of the modelled domain. The average standard deviation of inferred crustal velocities is generally less than ∼0.1 km/s.

The crust thickens from ∼25 km in the Thurston Island block (PIG3), to ∼29 km at the Haag Nunataks (FOWL), to ∼37 km in the Ellsworth Mountains (node 1624). In the southern Antarctic Peninsula (BREN) the crust is ∼39 km; however, this profile is the least well constrained of those displayed due to the peripheral location (see Figures 1 and 5). The crust is ∼27 km thick in MBL (SILY), ∼26 km in the central WARS (BYRD), and ∼36 km thick at the Dufek Intrusion (DUFK). The signature of a sharp crust-mantle transition is absent at the southern TAM front (SURP), so the estimated crustal thickness of ∼26 km is less well constrained than the other locations. These estimates of crustal thickness are consistent with preceding studies (e.g., Chaput et al., 2014; Ramirez et al., 2017; O'Donnell et al., 2017).

All V_{SV} depth profiles show a high-velocity seismic mantle "lid". Defining the seismic lithosphere-asthenosphere boundary (LAB) at the strongest negative velocity gradient at the base of the high-velocity lid (e.g., Eaton et al., 2009), the seismic LAB is at ∼85 km depth beneath the Thurston Island block (PIG3), MBL (SILY), the central WARS (BYRD) and southern TAM front (SURP). The seismic LAB depth increases to ∼92 km at the Dufek Intrusion (DUFK) and ∼96 km at the Ellsworth Mountains (node 1624) (Figure 7). Alternative definitions of the seismic LAB exist (e.g., Eaton et al., 2009); for example, adopting the onset of the negative velocity gradient at the lid base would reduce our seismic LAB depth estimates by ∼10-20 km. The lid at the southern TAM front (SURP), and at MBL (SILY) to a lesser extent, is underlain

by a pronounced low velocity zone: at ∼130 km depth, V_{SV} is ∼4.05-4.15 km/s at SURP and ∼4.15-4.20 km/s at SILY. In contrast to SURP and SILY, at BYRD in the central WARS V_{SV} is ∼4.20-4.30 km/s at 130 km depth.

2D V_{SV} maps were constructed by gridding the suite of 1D V_{SV} profiles (Figures 8 and 9). At 25 km depth, velocities strongly characteristic of crustal lithologies (V_{SV} <∼4.0 km/s) are evident beneath the southern TAM, the WSRS, the HEW block and the Antarctic Peninsula. The slowest velocities at this depth are located beneath the southern TAM and Ellsworth Mountains. However, the ANT resolution degrades on the Peninsula (O'Donnell et al., 2018), so the inferred crustal V_{SV} velocities there are likely overestimated; gravity data suggest that crustal thickness on the southern Peninsula is comparable to that beneath the Ellsworth Mountains (e.g., O'Donnell & Nyblade, 2014). Faster velocities - indicative of thinner crust - characterise the WARS at this depth, with velocities indicative of mantle rock (V_{SV} >∼4.3 km/s) apparent in the Ross and Amundsen Sea Embayments. Crust thinner than 25 km at these locations is consistent with preceding studies (e.g., Chaput et al., 2014; Shen et al., 2018). Our model suggests that thicker crust in the WARS is found in a region extending south from the MBL topographic dome, consistent with Chaput et al. (2014).

The outstanding feature at 60 km depth is the high velocity anomaly located between the Ellsworth Mountains and the Dufek Intrusion/Pensacola Mountains, also seen in cross-section AA' in Figure 9. Storey & Kyle (1997) posit that plume-generated Ferrar magmas could have ponded in large magma chambers, like that from which the Dufek Intrusion crystallized (see Figure 1 for location), and from these spread along the length of the TAM, explaining the chemical uniformity of Ferrar exposures over large distances. Shear velocities of the magnitude we infer (∼4.6-4.8 km/s) in the lithospheric mantle beneath the southern WSRS are characteristic of depleted, cratonic lithosphere. We speculate that the high velocity anomaly might reflect depleted

mantle lithosphere following the extraction of voluminous melt related to Gondwana breakup.

The absence of a sharp velocity contrast at the eastern margin of the WSRS is consistent with the WSRS being a broad extensional/transtensional province within a distributed plate boundary between East and West Antarctica (Jordan et al., 2017). The conventional interpretation of the TAM as the margin of East Antarctica in the Weddell Sea Embayment may need to be re-visited.

The seismic signature of the cratonic margin of East Antarctic is clear along the southern and northern TAM front at depth slices 120 and 150 km. However, the boundary is located behind the southern TAM front. Depth slices at 90, 120 and 150 km reveal a pronounced low velocity anomaly underlying the southern TAM front (minimum V_{SV} is ~4.05 km/s). Shen et al. (2017, 2018) also image this low velocity anomaly and attribute it to lithospheric foundering, a mechanism they invoke to explain the uplift of the TAM. The southern portions of our cross-sections CC' and DD' in Figure 9 does not contradict their interpretation. Taken together with a magnetotelluric study advocating flexural support of the central TAM by thick, high electrical resistivity lithosphere (Wannamaker et al., 2017), and seismic studies advocating flexural support of the northern TAM by warm, buoyant upper mantle impinging from the adjacent WARS (e.g., Lawrence et al., 2006), this points to along-strike variation in the tectonic history of the TAM.

We do not interpret structure below 200 km depth, but seismic velocities characteristic of cratonic lithosphere are inferred to persist to depths of ~220-250 km beneath East Antarctica (e.g., Ritzwoller et al., 2001; Shen et al., 2018). The thickness of the seismic lid beneath the Ellsworth Mountains (~95-100 km) is substantially less than that underlying the East Antarctic craton (see cross-section AA in Figure 9). This points to modification of the Precambrian lithosphere beneath the Ellsworth Whitmore Mountains, which Lloyd et al. (2015) suggest reflects lithospheric foundering

related to Gondwana breakup, magmatic intrusion, and subsequent development of the WARS.

At 90 km depth, high velocity zones (V_{SV} ~4.5-4.55 km/s) are apparent south of the MBL dome and in the eastern Ross Sea Embayment. White-Gaynor et al. (2019) propose that relatively faster upper mantle V_P velocities imaged beneath the eastern Ross Sea Embayment by body-wave tomography reflect lithosphere that may not have been reheated by the Cenozoic rifting that affected other parts of the WARS. Xenolith analyses suggest that lithospheric mantle beneath MBL and circum-Pacific Phanerozoic continental crustal terranes in south east Australia and other locations in Zealandia preserves ancient Archean-Proterozoic peridotite components (e.g., Handler et al., 2003; Liu et al., 2015, and references therein). Handler et al. (2003) suggest that the Proterozoic mantle beneath MBL might have a provenance in the East Antarctic craton, while Liu et al. (2015) invoke a model whereby ancient depleted mantle domains are dispersed in the convecting mantle and reappear beneath young continents. As a possible alternative to the White-Gaynor et al. (2019) model, we suggest that the high velocity zones imaged south of the MBL dome and in the eastern Ross Sea Embayment might reflect the compositional signature of ancient continental fragments.

Cenozoic alkaline volcanism in MBL, which started at ~28-30 Ma, was preceded by uplift of the peneplained surface of the MBL block. This, and the isotopic signature of a high-U/Pb (HIMU) mantle reservoir in the rocks, suggests plume-related volcanism (e.g., LeMasurier & Landis, 1996, and references therein). Anomalously low seismic velocity upper mantle beneath the MBL dome is consistently imaged, but the unambiguous signature of a plume "tail" extending deeper into the mantle has thus far evaded detection (e.g., Lloyd et al., 2015; Shen et al., 2018). At the northern margin of the WARS, we image a pronounced low velocity anomaly stretching eastward from beneath the MBL dome to Pine Island Bay, underlying Thwaites

Glacier, but not Pine Island Glacier. The velocity contrast between this perturbed upper mantle and that of the inner WARS (∼5%) is consistent with estimates from Lloyd et al. (2015) and Shen et al. (2018). Assuming temperature is the dominant control on lateral variations in seismic velocity in the upper mantle, this contrast translates to a thermal anomaly of ∼125-200 °C (e.g., Faul & Jackson, 2005). Finn et al. (2005) favour a model of subduction-related alkaline magma genesis in MBL. They suggest that protracted Paleozoic-Mesozoic subduction along the Paleo-Pacific margin of Gondwana resulted in metasomatic enrichment of the upper mantle; detachment of subducted slabs in the late Cretaceous along the former Gondwana margin induced Rayleigh-Taylor instabilities, triggering lateral and vertical flow of warm Pacific mantle. They suggest that this catalysed melting of the metasomatised upper mantle, resulting in Cenozoic alkaline magmatism. Emry et al. (2014) also suggest that subduction-related volatiles might explain negative peaks in receiver functions above the mantle transition zone in West Antarctica. The velocity anomaly we image strikes approximately parallel to the convergent paleo-Pacific margin of Gondwana, so it conceivably encodes the signature of subduction-related melt and volatiles rather than, or in addition to, plume-related anomalously elevated temperatures. Additional data (e.g., compressional wave velocities, resistivity measurements) are needed to differentiate between chemical and thermal contributions to the observed low shear wave velocity anomaly, and hence between subduction and plume hypotheses. A less pronounced low velocity zone underlying the southern Antarctica Peninsula to ∼100 km depth may similarly encode the signature of Mesozoic subduction and/or a remnant thermal signature of the mid-Cretaceous Palmer Land orogeny affecting the southern Peninsula (e.g., Vaughan et al., 2002).

A low velocity anomaly underlying the Bentley Subglacial Trench in the central WARS is evident at depth slices 90, 120 and 150 km (minimum V_{SV} is ∼4.15-4.20 km/s). Lloyd et al. (2015) imaged the same velocity anomaly, arguing that it represents

a thermal anomaly associated with focussed Neogene extension. They suggest that surrounding faster velocities in the WARS may reflect Late Cretaceous/early Cenozoic extension whose thermal perturbation due to rifting has largely dissipated.

The V_{SV} maps suggests that - the Bentley Subglacial Trench aside - current tectonism in the WARS is concentrated beneath the rift margins. By 180 km depth, lateral variations in velocity across West Antarctica are much reduced, as is the contrast with East Antarctica. The reduced lateral velocity variations within West Antarctica suggest that rift-related tectonism is largely confined to the uppermost mantle (<180 km depth).

6.2 Geotherms and Heat Flow

Accurate estimation of geothermal heat flow in West Antarctica is pressing given the considered vulnerability of the WAIS to marine ice sheet instability (e.g., Barletta et al., 2018). We seek the steady-state conductive geotherms, and hence surface heat flows, best explaining inferred V_{SV} profiles at representative tectonic locations in West Antarctica. The selected stations/grid nodes have V_{SV} profiles typical of their parent tectonic domains: the southern Antarctic Peninsula (BREN), the central WARS (BYRD), the Thurston Island block (PIG3, located adjacent to Pine Island Glacier), and the Ellsworth Mountains of the HEW block (grid node 1624) (Figure 7). Based on the location of low V_{SV} velocity anomalies in Figure 8, steady-state conduction is probably a reasonable assumption at these locations. Locations for which steady-state conduction is unlikely, for example, in MBL and the southern TAM, are beyond the scope of the present study. A companion study to define 3D variations in mantle viscosity beneath West Antarctica will use the V_{SV} model as a 3D gauge of uppermost mantle temperatures.

We use the Abers & Hacker (2016) MATLAB toolbox to predict the elastic, isotropic

V_S of average spinel peridotite and garnet peridotite compositions of lithospheric mantle for candidate geotherms. The spinel peridotite composition represents average continental lithospheric mantle based on spinel lherzolite xenoliths (McDonough, 1990), and the garnet peridotite composition represents "tecton" (i.e., formed or modified at < 1 Ga) lithospheric mantle based on garnet xenocrysts (Griffin et al., 2009). For fertile peridotites, the transition from spinel peridotite to garnet peridotite occurs at ∼1.5 GPa (∼45-50 km depth) (e.g., Lee, 2003, and references therein).

For a layer of thickness Δz with constant radiogenic heat production, A, and constant thermal conductivity, k, undergoing 1D steady-state heat conduction, the temperature and heat flow at the bottom of the layer (T_b and q_b, respectively) can be determined from the temperature and heat flow at the top of the layer (T_t and q_t, respectively) using

$$T_b = T_t + \frac{q_t}{k}\Delta z - \frac{A}{2k}\Delta z^2 \tag{1}$$

and

$$q_b = q_t - A\Delta z \tag{2}$$

(e.g., Hasterok & Chapman, 2011; Furlong & Chapman, 2013). A 1D steady-state conductive geotherm is obtained by applying these equations to successive layers and iterating to account for the temperature and pressure dependence of thermal conductivity.

Under steady-state conditions, surface heat flow represents the sum of heat flow into the base of the lithosphere and the integrated radiogenic heat production within the lithosphere. Direct measurement of radiogenic heat production indicates generally high values in felsic rocks (∼2-3 μW/m^3), low values in mafic rocks (∼0.2 μW/m^3), and very low values in ultramafic rocks (∼0.02 μW/m^3) (e.g., Furlong & Chapman, 2013). We segregate our 1D V_{SV} crustal profiles into upper (felsic) and lower (mafic) portions based on the observed velocities, with each portion comprising a sequence

of 1 km thick layers (i.e., $\Delta z = 1\,\mathrm{km}$). A global compilation of seismic velocities suggests that middle continental crust is dominated by $V_P = 6.5\text{-}6.8\,\mathrm{km/s}$ and $V_P/V_S = 1.65\text{-}1.80$ (Hacker et al., 2015), implying an upper-middle crust transition at $V_S = 3.61\text{-}3.78\,\mathrm{km/s}$. We adopt $V_{SV} < 3.7\,\mathrm{km/s}$ as indicative of upper crust and $V_{SV} > 3.7\,\mathrm{km/s}$ as indicative of combined middle and lower crust - hereafter referred to as lower crust. To the lower crust we assign a heat production of $0.4\,\mu\mathrm{W/m^3}$ (e.g., Hasterok & Chapman, 2011). We regard $V_{SV} > 4.3\,\mathrm{km/s}$ as defining the transition to the lithospheric mantle, where we fix heat production at $0.02\,\mu\mathrm{W/m^3}$ (e.g., Hasterok & Chapman, 2011; Furlong & Chapman, 2013). Upper crustal heat production, A_{UC}, is assigned according to

$$A_{UC} = (1 - F)q_S/D, \tag{3}$$

where D is the thickness of the upper crust (defined by $V_{SV} < 3.7\,\mathrm{km/s}$), q_S is surface heat flow and F is a partition coefficient defining the ratio of "basal" heat flow (the combination of middle/lower crustal heat production, lithospheric mantle heat production, and sub-lithospheric heat flow) to surface heat flow (e.g., Hasterok & Chapman, 2011; Furlong & Chapman, 2013). With observed seismic velocities controlling the definition of upper crustal, lower crustal and lithospheric mantle layers, the partition model facilitates the convenient parameterisation of steady-state geotherms in terms of a single variable: surface heat flow. Using a preferred partition coefficient of $F = 0.74$ (Hasterok & Chapman, 2011), we vary q_S in increments of $5\,\mathrm{mW/m^2}$ to produce candidate steady-state conductive geotherms at locations representative of the southern Antarctic Peninsula (BREN), the central WARS (BYRD), the Thurston Island block in the vicinity of Pine Island Glacier (PIG3), and the Ellsworth Mountains in the HEW block (grid node 1624). Crustal thermal conductivity is calculated following Furlong & Chapman (2013) and lattice and radiative contributions to thermal conductivity in the lithospheric mantle calculated following Hasterok & Chapman (2011).

Attendant elastic, isotropic V_S velocities for the lithospheric mantle are calculated from the geotherms using Abers & Hacker (2016). To facilitate comparison with the observed anelastic, V_{SV} velocities, the calculated velocities are converted to anelastic, V_{SV} velocities assuming PREM Q values and 4% radial anisotropy in the lithospheric mantle of West Antarctica (Ritzwoller et al., 2001). We do not attempt to model the crustal velocity profiles due to the more complex compositional heterogeneity.

Figure 10 shows geotherms best explaining the observed V_{SV} profiles for the Antarctic Peninsula (BREN), the central WARS (BYRD), the Ellsworth Mountains of the HEW block (node 1624), and the Thurston Island block in the vicinity of Pine Island Glacier (PIG3). We present geotherms corresponding to lower-bound, upper-bound and preferred heat flows.

For a tecton garnet peridotite composition, a surface heat flow of $\sim$60 mW/m^2 at BYRD and PIG3 and $\sim$50 mW/m^2 at node 1624 yield geotherms that explain the inferred V_{SV} of the lower lithospheric mantle reasonably well. We define the thermal LAB as the intersection of the conductive geotherm and a mantle adiabat based on a mantle potential temperature of 1300°C and adiabatic temperature gradient of 0.45°C/km (e.g., Katsura et al., 2010). While the seismic and thermal LABs need not coincide (e.g., Eaton et al., 2009), they do covary and occur within $\sim$5-15 km of each other at these locations for our preferred heat flows. The V_{SV} profile of the upper lithospheric mantle at these three locations is more problematic. At PIG3 and node 1624 in particular, the predicted upper lithospheric mantle V_{SV} is beyond one standard deviation of the observed mean V_{SV} for the garnet peridotite composition. The spinel peridotite composition reduces the predicted V_{SV} somewhat, but a discrepancy persists. Potential contributors to the discrepancy include (1) inadequate capture of the true velocity structure at the crust-mantle transition, (2) the adoption of constant radial anisotropy of strength 4% in the lithospheric mantle, (3) the use of PREM Q values to convert from elastic to anelastic velocities, (4) the assumed spinel

peridotite and garnet peridotite compositions, and (5) the partition model of heat production. Surface waves are less sensitive to sharp impedance contrasts than they are to average velocity structure. The addition of receiver function data would better constrain velocity structure at the crust-mantle transition (e.g., Shen et al., 2018) and mitigate (1). Within the remit of Antarctic seismology, the development of Love wave and attenuation tomography models would eliminate the need for assumptions (2) and (3), respectively.

Our preferred surface heat flow of $\sim$60 mW/m^2 at BYRD is largely consistent with inferences based on satellite magnetic data ($\sim$55-65 mW/m^2; Fox Maule et al., 2005) and seismic data ($\sim$70 mW/m^2; An et al., 2015a)) at that location, and an inferred broad scale heat flow of 60-70 mW/m^2 for east-central West Antarctica based on magnetotelluric data (Wannamaker et al., 2017). Our preferred surface heat flow of $\sim$60 mW/m^2 is similarly broadly consistent with a heat flow of $\sim$60-65 mW/m^2 inferred by geodynamic modelling of WARS evolution (van Wijk et al., 2008) and a heat flow of 70 mW/m^2 invoked as representative of Mesozoic-Cenozoic rifts for Antarctic ice sheet modelling (Pollard et al., 2005). A slightly higher heat flow of $\sim$75 mW/m^2 at BYRD was estimated from a drill core through the ice sheet to bedrock (Gow et al., 1968). These values contrast with inferred heat flows in the central WARS of $\sim>$120 mW/m^2 based on airborne magnetic data (Martos et al., 2017) and $\sim$110 mW/m^2 based on the extrapolation of global heat flow measurements to Antarctica via seismic structural similarity (Shapiro & Ritzwoller, 2004).

Our preferred heat flow of $\sim$60 mW/m^2 at PIG3 is broadly consistent with inferences from satellite magnetic data ($\sim$55-65 mW/m^2; Fox Maule et al., 2005), seismic data ($\sim$70 mW/m^2; An et al., 2015a), airborne magnetic data ($\sim$60-75 mW/m^2; Martos et al., 2017), and in situ measurements in continental shelf sediments in the Amundsen Sea Embayment (mean $\sim$65 mW/m^2; Dziadek et al., 2019). Our preferred $\sim$60 mW/m^2 heat flow at PIG3 again contrasts with the $\sim$110 mW/m^2 modelled by

Shapiro & Ritzwoller (2004); however, their modelled standard deviations are of comparable magnitude to their inferred heat flows.

Our preferred heat flow of $\sim$50 mW/m^2 at node 1624 in the Ellsworth Mountains is lower than estimates based on satellite magnetic data ($\sim$70 mW/m^2; Fox Maule et al., 2005) and airborne magnetic data ($\sim$65-70 mW/m^2; Martos et al., 2017), but reasonably consistent with recent seismic-based inferences ($\sim$55 mW/m^2; An et al., 2015a). High heat producing granites in the upper crust are known to occur in the Ellsworth Mountains (e.g., Leat et al., 2018), a factor which might render the partition model of heat production with F = 0.74 inappropriate for modelling the local thermal regime.

A surface heat flow of $\sim$60 mW/m^2 best explains the observed V_{SV} profiles at BREN. The signature of a clear seismic LAB at BREN is lacking, likely a reflection of the degradation in resolution at the model periphery, but $q_S = 60$ mW/m^2 gives a thermal LAB of $\sim$85 km. Burton-Johnson et al. (2017) used geological analyses to infer a mean heat flow of 81 mW/m^2 on the east and south of the Antarctic Peninsula where silicic rocks predominate, and a mean of 67 mW/m^2 on the west and north where volcanic arc and quartzose sediments dominate. BREN is located approximately on the border between these domains, where the heat flow inferred by Burton-Johnson et al. (2017) is $\sim$60-80 mW/m^2. Martos et al. (2017) broadly replicate the spatial variation in heat flow on the Peninsula, but their inferred values are consistently higher than those of Burton-Johnson et al. (2017).

We emphasise that inferred heat flows are regional average (many hundreds of km) estimates constrained by seismic data with limited sensitivity to the upper crust in conjunction with radiogenic heat productions for felsic, mafic and ultramafic lithologies taken from global compilations (e.g., Hasterok & Chapman, 2011; Furlong & Chapman, 2013). This precludes meaningful comparison with geographically localised high heat flow anomalies (e.g., Fisher et al., 2015), but does not contradict such mea-

surements. Our inferred geotherms and heat flows can serve as regional average benchmarks which can be modified according to local conditions.

7 Conclusions

In this work, we combined data from the UKANET, POLENET-ANET, ASAIN, SEPA and GSN seismic arrays to construct from fundamental mode Rayleigh wave phase velocities a 3D shear wave velocity model of the West Antarctic upper mantle to 200 km depth. Our goals were (i) image and interpret structures against the tectonic evolution of West Antarctica, and (ii) extract information from the seismic model that can serve as boundary conditions in ice sheet and GIA modelling efforts.

We speculate that a high velocity anomaly located in the southern WSRS might reflect depleted mantle lithosphere following the extraction of voluminous melt related to Gondwana fragmentation. High velocity anomalies imaged by body-wave tomography in the upper mantle beneath the eastern Ross Sea Embayment have been interpreted as lithosphere that may not have been reheated by the Cenozoic rifting that affected other parts of the WARS (White-Gaynor et al., 2019). Motivated by xenolith analyses, as an alternative model we propose that high velocity zones imaged south of the MBL dome and in the eastern Ross Sea Embayment in this study might reflect the compositional signature of ancient continental fragments.

While the seismic signature of the cratonic margin of East Antarctic is clear along the southern and northern TAM, the absence of a sharp velocity contrast between the WSRS and East Antarctica is consistent with the WSRS being a broad extensional/transtensional province within a distributed plate boundary between East and West Antarctica (Jordan et al., 2017).

A pronounced low velocity anomaly underlying the southern TAM is consistent with a published lithospheric foundering hypothesis. Taken together with a magnetotelluric

study advocating flexural support of the central TAM by thick, stable lithosphere (Wannamaker et al., 2017), this points to along-strike variation in the tectonic history of the TAM.

The Bentley Subglacial Trench aside - which may have experienced a pulse of Neogene extension (Lloyd et al., 2015) - the distribution of low velocity anomalies suggests that current tectonism in the WARS is concentrated beneath the rift margins and largely confined to the uppermost mantle (<180 km depth). On the northern margin of the WARS, a pronounced low velocity anomaly extends eastward from beneath the MBL dome toward Pine Island Bay. If of plume-related thermal origin, the velocity contrast of ∼5% between this anomaly and the inner WARS translates to a temperature difference of ∼125-200 °C. However, the strike of the anomaly parallels the paleo-Pacific convergent margin of Gondwana, so it conceivably encodes the signature of subduction-related melt and volatiles rather than anomalously elevated temperatures, or a combination thereof. Thermal versus chemical origins will have different implications for geothermal heat flow and mantle viscosity modelling efforts to monitor and predict ice sheet evolution. Differentiating between them should be a pressing concern given that the anomaly underlies Thwaites Glacier, a major outlet glacier of the WAIS considered vulnerable to marine ice sheet instability (e.g., Barletta et al., 2018).

Lithospheric thickness estimates extracted from 1D shear wave velocity profiles representative of tectonic domains in West Antarctica indicate an average lithospheric thickness of ∼85 km for the WARS, MBL, and Thurston Island block. This increases to ∼96 km in the Ellsworth Mountains. ∼60 mW/m^2 geotherms best explain lithospheric mantle shear wave velocities in the central WARS (BYRD) and adjacent to Pine Island Glacier in the Thurston Island block (PIG3); a ∼50 mW/m^2 geotherm best explains the velocities in the Ellsworth Mountains (node 1624) and a ∼60 mW/m^2 geotherm best explains a less well-constrained velocity profile on the

southern Antarctic Peninsula (1624). We emphasise that inferred heat flows are regional average estimates constrained by seismic data with limited sensitivity to the upper crust. They do not preclude geographically-localised elevated heat flows due to localised Cenozoic extension or magmatic activity or variations in upper crustal heat production rooted in compositional variation.

8 Acknowledgements

We thank all BAS camp staff, field guides and air unit personnel for the logistical support of the UKANET seismic and GNSS networks. We similarly acknowledge all field teams and camp staff associated with the POLENET-ANET project, and thank Kenn Borek Air and the New York Air Guard for flight support. JPOD, GAN and PLW are supported by the Natural Environment Research Council [grants NE/L006065/1, NE/L006294/1 and NE/K009958/1], KS is supported by the Australia Research Council [grant F150100541]. POLENET-ANET is supported by the National Science Foundation Office of Polar Programs [grants 0632230, 0632239, 0652322, 0632335, 0632136, 0632209, and 0632185]. UKANET seismic instrumentation was provided and supported by SEIS-UK. POLENET-ANET seismic instrumentation was provided and supported by the Incorporated Research Institutions for Seismology (IRIS) through the PASSCAL Instrument Center. The UKANET (`www.ukanet.wixsite.com/ukanet`; network code 1D; `https://doi.org/10.7914/SN/1D_2016`) data will be accessible through the IRIS Data Management Center (`http://www.iris.edu/mda`) from January 2021. POLENET-ANET (network code YT), ASAIN (network code AI), GSN (network code IU) and SEPA (network code XB) seismic data can be accessed through the IRIS DMC. The facilities of the IRIS Consortium are supported by the NSF under cooperative agreement EAR-1063471, the NSF Office of Polar Programs, and the DOE National Nuclear Security Admin-

istration. Figures were created using the Generic Mapping Tools (GMT) software (http://gmt.soest.hawaii.edu). The phase and shear wave velocity models developed here can be accessed at the UK Polar Data Centre (https://doi.org/10.5285/c11bdb27-df44-4b56-8f4c-afc51b6e1e3a and https://doi.org/10.5285/b5ffac8a-9846-4f86-9a71-3ce992a18148).

References

Abers, G. A. & Hacker, B. R., 2016. A MATLAB toolbox and Excel workbook for calculating the densities, seismic wave speeds, and major element composition of minerals and rocks at pressure and temperature, *Geochem. Geophys. Geosyst.*, **17**(2), 616–624, doi:10.1002/2015GC006171.

An, M., Wiens, D. A., Zhao, Y., Feng, M., Nyblade, A., Kanao, M., Li, Y., Maggi, A., & Lévêque, J.-J., 2015a. Temperature, lithosphere-asthenosphere boundary, and heat flux beneath the Antarctic Plate inferred from seismic velocities, *J. Geophys. Res.*, **120**(12), 8720–8742, doi:10.1002/2015JB011917.

An, M., Wiens, D. A., Zhao, Y., Feng, M., Nyblade, A. A., Kanao, M., Li, Y., Maggi, A., & Lévêque, J.-J., 2015b. S-velocity model and inferred Moho topography beneath the Antarctic Plate from Rayleigh waves, *J. Geophys. Res.*, **120**(1), 359–383.

Barletta, V. R., Bevis, M., Smith, B. E., Wilson, T., Brown, A., Bordoni, A., Willis, M., Khan, S. A., Rovira-Navarro, M., Dalziel, I., Smalley, R., Kendrick, E., Konfal, S., Caccamise, D. J., Aster, R. C., Nyblade, A., & Wiens, D. A., 2018. Observed rapid bedrock uplift in Amundsen Sea Embayment promotes ice-sheet stability, *Science*, **360**(6395), 1335–1339, doi:10.1126/science.aao1447.

Birch, F., 1961. The velocity of compressional waves in rocks to 10 kilobars, part 2, *J. Geophys. Res.*, **66**(7), 2199–2224.

Brocher, T. M., 2005. Empirical Relations between Elastic Wavespeeds and Density in the Earth's Crust, *Bull., Seis. Soc. Am.*, **95**(6), 2081.

Burton-Johnson, A., Halpin, J. A., Whittaker, J. M., Graham, F. S., & Watson, S. J., 2017. A new heat flux model for the Antarctic Peninsula incorporating spatially

variable upper crustal radiogenic heat production, *Geophys. Res. Lett.*, **44**(11), 5436–5446, doi:10.1002/2017GL073596.

Chaput, J., Aster, R. C., Huerta, A., Sun, X., Lloyd, A., Wiens, D., Nyblade, A., Anandakrishnan, S., Winberry, J. P., & Wilson, T., 2014. The Crustal Thickness of West Antarctica, *J. Geophys. Res.*, **119**, 1–18, doi:10.1002/2013JB010642.

Dalziel, I. W. D., 1992. Antarctica: A tale of two supercontinents?, *Annu. Rev. Earth Pl. Sc.*, **20**, 501–526.

Dalziel, I. W. D. & Elliot, D. H., 1982. West Antarctica: Problem child of Gondwanaland, *Tectonics*, **1**(1), 3–19, doi:10.1029/TC001i001p00003.

Dziadek, R., Gohl, K., Kaul, N., & Science Team of Expedition PS1041, 2019. Elevated geothermal surface heat flow in the Amundsen Sea Embayment, West Antarctica, *Earth Planet. Sci. Lett.*, **506**, 530–539, doi:10.1016/j.epsl.2018.11.003.

Dziewonski, A. M. & Anderson, D. L., 1981. Preliminary reference Earth model, *Phys. Earth Planet. Int.*, **25**(4), 297–356.

Eaton, D. W., Darbyshire, F., Evans, R. L., Grütter, H., Jones, A. G., & Yuan, X., 2009. The elusive lithosphere-asthenosphere boundary (LAB) beneath cratons, *Lithos*, **109**(1-2), 1–22.

Emry, E. L., Nyblade, A. A., Julià, J., Anandakrishnan, S., Aster, R. C., Wiens, D. A., Huerta, A. D., & Wilson, T. J., 2014. The mantle transition zone beneath West Antarctica: Seismic evidence for hydration and thermal upwellings, *Geochem. Geophys. Geosyst.*, **16**(1), 40–58, doi:10.1002/2014GC005588.

Faul, U. H. & Jackson, I., 2005. The seismological signature of temperature and grain size variations in the upper mantle, *Earth Planet. Sci. Lett.*, **234**, 119–134.

Finn, C. A., Müller, R. D., & Panter, K. S., 2005. A Cenozoic diffuse alkaline magmatic province (DAMP) in the southwest Pacific without rift or plume origin, *Geochem. Geophys. Geosyst.*, **6**(2), doi:10.1029/2004GC000723.

Fisher, A. T., Mankoff, K. D., Tulaczyk, S. M., Tyler, S. W., Foley, N., & the WISSARD science team, 2015. High geothermal heat flux measured below the West Antarctic Ice Sheet, *Sci. Adv.*, **1**(6), doi:10.1126/sciadv.1500093.

Fitzgerald, P., 2002. Tectonics and landscape evolution of the Antarctic plate since the breakup of Gondwana, with an emphasis on the West Antarctic Rift System and the Transantarctic Mountains, *Royal Society of New Zealand Bulletin*, **35**, 453–469.

Forysth, D. W. & Li, A., 2005. Array analysis of two-dimensional variations in surface wave phase velocity and azimuthal anisotropy in the presence of multipathing interference, in Seismic Earth: Array Analysis of Broadband Seismograms, Geophys. Monogr. Ser. 157, pp. 81–97, eds Levander, A. & Nolet, G., American Geophysical Union, Washington, DC, doi:10.1029/157GM06.

Fox Maule, C., Purucker, M. E., Olsen, N., & Mosegaard, K., 2005. Heat Flux Anomalies in Antarctica Revealed by Satellite Magnetic Data, *Science*, **309**(5733), 464–467.

Fretwell, P., Pritchard, H. D., Vaughan, D. G., Bamber, J. L., Barrand, N. E., Bell, R., Bianchi, C., Bingham, R. G., Blankenship, D. D., Casassa, G., Catania, G., Callens, D., Conway, H., Cook, A. J., Corr, H. F. J., Damaske, D., Damm, V., Ferraccioli, F., Forsberg, R., Fujita, S., Gim, Y., Gogineni, P., Griggs, J. A., Hindmarsh, R. C. A., Holmlund, P., Holt, J. W., Jacobel, R. W., Jenkins, A., Jokat, W., Jordan, T., King, E. C., Kohler, J., Krabill, W., Riger-Kusk, M., Langley, K. A., Leitchenkov, G., Leuschen, C., Luyendyk, B. P., Matsuoka, K., Mouginot, J., Nitsche, F. O.,

689 Nogi, Y., Nost, O. A., Popov, S. V., Rignot, E., Rippin, D. M., Rivera, A., Roberts,
690 J., Ross, N., Siegert, M. J., Smith, A. M., Steinhage, D., Studinger, M., Sun, B.,
691 Tinto, B. K., Welch, B. C., Wilson, D., Young, D. A., Xiangbin, C., & Zirizzotti, A.,
692 2013. Bedmap2: improved ice bed, surface and thickness datasets for Antarctica,
693 *The Cryosphere*, **7**, 375–393, doi:10.5194/tc-7-375-2013.

694 Furlong, K. P. & Chapman, D. S., 2013. Heat Flow, Heat Generation, and the
695 Thermal State of the Lithosphere, *Annu. Rev. Earth Pl. Sc.*, **41**(1), 385–410,
696 doi:10.1146/annurev.earth.031208.100051.

697 Gow, A. J., Ueda, H. T., & Garfield, D. E., 1968. Antarctic ice sheet: Preliminary
698 results of first core hole to bedrock, *Science*, **161**(3845), 1011–1013.

699 Griffin, W. L., O'Reilly, S. Y., Afonso, J. C., & Begg, G. C., 2009. The Composition
700 and Evolution of Lithospheric Mantle: a Re-evaluation and its Tectonic Implica-
701 tions, *J. Petrol.*, **50**(7), 1185–1204, doi:10.1093/petrology/egn033.

702 Guo, Z., Chen, Y. J., Ning, J., Yang, Y., Afonso, J. C., & Tang, Y., 2016. Seismic evi-
703 dence of on-going sublithosphere upper mantle convection for intra-plate volcanism
704 in Northeast China, *Earth Planet. Sci. Lett.*, **433**, 31–43.

705 Hacker, B. R., Kelemen, P. B., & Behn, M. D., 2015. Continental lower crust, *Annual*
706 *Review of Earth and Planetary Sciences*, **43**(1), 167–205, doi:10.1146/annurev-
707 earth-050212-124117.

708 Handler, M. R., Wysoczanski, R. J., & Gamble, J. A., 2003. Proterozoic lithosphere
709 in Marie Byrd Land, West Antarctica: Re-Os systematics of spinel peridotite xeno-
710 liths, *Chem. Geol.*, **196**(1-4), 131–145, doi:10.1016/S0009-2541(02)00410-2.

711 Hasterok, D. & Chapman, D., 2011. Heat production and geotherms
712 for the continental lithosphere, *Earth Planet. Sci. Lett.*, **307**(1), 59–70,
713 doi:10.1016/j.epsl.2011.04.034.

Heeszel, D. S., Wiens, D. A., Anandakrishnan, S., Aster, R. C., Dalziel, I. W. D., Huerta, A. D., Nyblade, A. A., Wilson, T. J., & Winberry, P., 2016. Upper mantle structure of central and West Antarctica from array analysis of Rayleigh wave phase velocities, *J. Geophys. Res.*, doi:10.1002/2015JB012616.

Jordan, T., Ferraccioli, F., & Leat, P., 2017. New geophysical compilations link crustal block motion to Jurassic extension and strike-slip faulting in the Weddell Sea Rift System of West Antarctica, *Gondwana Research*, **42**, 29–48, doi:10.1016/j.gr.2016.09.009.

Katsura, T., Yoneda, A., Yamazaki, D., Yoshino, T., & Ito, E., 2010. Adiabatic temperature profile in the mantle, *Phys. Earth Planet. Int.*, **183**(1-2), 212–218, doi:10.1016/j.pepi.2010.07.001.

Lawrence, J. F., Wiens, D. A., Nyblade, A. A., Anandakrishnan, S., Shore, P., & Voigt, D., 2006. Crust and upper mantle structure of the Transantarctic Mountains and surrounding regions from receiver functions, surface waves, and gravity: Implications for uplift models, *Geochem. Geophys. Geosyst.*, **7**(10), doi:10.1029/2006GC001282.

Leat, P. T., Jordan, T. A., Flowerdew, M. J., Riley, T. R., Ferraccioli, F., & Whitehouse, M. J., 2018. Jurassic high heat production granites associated with the Weddell Sea rift system, Antarctica, *Tectonophysics*, **722**, 249–264, doi:10.1016/j.tecto.2017.11.011.

Lee, C.-T. A., 2003. Compositional variation of density and seismic velocities in natural peridotites at STP conditions: Implications for seismic imaging of compositional heterogeneities in the upper mantle, *J. Geophys. Res.*, **108**(B9), doi:10.1029/2003JB002413.

LeMasurier, W. E. & Landis, C. A., 1996. Mantle-plume activity recorded by low-

relief erosion surfaces in West Antarctica and New Zealand, *Geol. Soc. Am. Bull.*, **108**(11), 1450–1466.

Liu, J., Scott, J. M., Martin, C. E., & Pearson, D. G., 2015. The longevity of Archean mantle residues in the convecting upper mantle and their role in young continent formation, *Earth Planet. Sci. Lett.*, **424**, 109–118, doi:10.1016/j.epsl.2015.05.027.

Lloyd, A. J., Wiens, D. A., Nyblade, A. A., Anandakrishnan, S., Aster, R. C., Huerta, A. D., Wilson, T. J., Dalziel, I. W. D., Shore, P. J., & Zhao, D., 2015. A seismic transect across West Antarctica: Evidence for mantle thermal anomalies beneath the Bentley Subglacial Trench and the Marie Byrd Land Dome, *J. Geophys. Res.*, **120**(12), 8439–8460, doi:10.1002/2015JB012455.

Martos, Y. M., Catalán, M., Jordan, T. A., Golynsky, A., Golynsky, D., Eagles, G., & Vaughan, D. G., 2017. Heat Flux Distribution of Antarctica Unveiled, *Geophys. Res. Lett.*, **44**(22), 11,417–11,426, doi:10.1002/2017GL075609.

McDonough, W., 1990. Constraints on the composition of the continental lithospheric mantle, *Earth Planet. Sci. Lett.*, **101**(1), 1–18, doi:10.1016/0012-821X(90)90119-I.

Nield, G. A., Whitehouse, P. L., van der Wal, W., Blank, B., O'Donnell, J. P., & Stuart, G. W., 2018. The impact of lateral variations in lithospheric thickness on glacial isostatic adjustment in West Antarctica, *Geophys. J. Int.*, **214**(2), 811–824, doi:10.1093/gji/ggy158.

O'Donnell, J. P. & Nyblade, A. A., 2014. Antarctica's hypsometry and crustal thickness: Implications for the origin of anomalous topography in East Antarctica, *Earth Planet. Sci. Lett.*, **388**, 143–155.

O'Donnell, J. P., Selway, K., Nyblade, A. A., Brazier, R. A., Wiens, D. A., Anandakrishnan, S., Aster, R. C., Huerta, A. D., Wilson, T., & Winberry, J. P., 2017. The

763 uppermost mantle seismic velocity and viscosity structure of central West Antarc-
764 tica, *Earth Planet. Sci. Lett.*, **472**, 38–49, doi:10.1016/j.epsl.2017.05.016.

765 O'Donnell, J. P., Dunham, C., Stuart, G. W., Brisbourne, A., Nield, G. A., White-
766 house, P. L., Hooper, A. J., Nyblade, A., Wiens, D., Aster, R. C., Anandakrishnan,
767 S., Huerta, A. D., Wilson, T. J., & Winberry, J. P., 2018. Geothermal Heat Flux
768 and Upper Mantle Viscosity across West Antarctica: Insights from the UKANET
769 and POLENET Seismic Networks, *AGU Fall Meeting Abstracts*.

770 Pollard, D., DeConto, R. M., & Nyblade, A. A., 2005. Sensitivity of Cenozoic Antarc-
771 tic ice sheet variations to geothermal heat flux, *Glob. Planet. Change*, **49**(1-2),
772 63–74.

773 Ramirez, C., Nyblade, A., Emry, E., Julià, J., Sun, X., Anandakrishnan, S., Wiens,
774 D., Aster, R., Huerta, A., Winberry, P., & Wilson, T., 2017. Crustal structure of the
775 Transantarctic Mountains, Ellsworth Mountains and Marie Byrd Land, Antarctica:
776 constraints on shear wave velocities, Poisson's ratios and Moho depths, *Geophys.*
777 *J. Int.*, **211**(3), 1328–1340.

778 Ritzwoller, M. H., Shapiro, N. M., Levshin, A. L., & Leahy, G. M., 2001. Crustal and
779 upper mantle structure beneath Antarctica and surrounding oceans, *J. Geophys.*
780 *Res.*, **106**(B12), 30645–30670, doi:10.1029/2001JB000179.

781 Shapiro, N. M. & Ritzwoller, M. H., 2004. Inferring surface heat flux distribu-
782 tions guided by a global seismic model: particular application to Antarctica, *Earth*
783 *Planet. Sci. Lett.*, **223**(1), 213–224, doi:10.1016/j.epsl.2004.04.011.

784 Shen, W., Wiens, D. A., Stern, T., Anandakrishnan, S., Aster, R. C., Dalziel, I.,
785 Hansen, S., Heeszel, D. S., Huerta, A., Nyblade, A., Wilson, T. J., & Winberry,
786 J. P., 2017. Seismic evidence for lithospheric foundering beneath the southern
787 Transantarctic Mountains, Antarctica, *Geology*, **46**(1), 71, doi:10.1130/G39555.1.

Shen, W., Wiens, D. A., Anandakrishnan, S., Aster, R. C., Gerstoft, P., Bromirski, P. D., Hansen, S. E., Dalziel, I. W. D., Heeszel, D. S., Huerta, A. D., Nyblade, A. A., Stephen, R., Wilson, T. J., & Winberry, J. P., 2018. The Crust and Upper Mantle Structure of Central and West Antarctica From Bayesian Inversion of Rayleigh Wave and Receiver Functions, *J. Geophys. Res.*, doi:10.1029/2017JB015346.

Storey, B. & Kyle, P., 1997. An active mantle mechanism for Gondwana breakup, *S. Afr. J. Geol.*, **100**(4), 283–290.

van Wijk, J., Lawrence, J., & Driscoll, N., 2008. Formation of the Transantarctic Mountains related to extension of the West Antarctic Rift system, *Tectonophysics*, **458**(1), 117–126, doi.org/10.1016/j.tecto.2008.03.009.

Vaughan, A. P. M., Kelley, S. P., & Storey, B. C., 2002. Mid-Cretaceous ductile deformation on the Eastern Palmer Land Shear Zone, Antarctica, and implications for timing of Mesozoic terrane collision, *Geol. Mag.*, **139**(4), 465–471, doi:10.1017/S0016756802006672.

Wannamaker, P., Hill, G., Stodt, J., Maris, V., Ogawa, Y., Selway, K., Boren, G., Bertrand, E., Uhlmann, D., Ayling, B., Green, A. M., & Feucht, D., 2017. Uplift of the central transantarctic mountains, *Nat. Commun.*, **8**(1), 1588.

White-Gaynor, A. L., Nyblade, A. A., Aster, R. C., Wiens, D. A., Bromirski, P. D., Gerstoft, P., Stephen, R. A., Hansen, S. E., Wilson, T., Dalziel, I. W., Huerta, A. D., Winberry, J. P., & Anandakrishnan, S., 2019. Heterogeneous upper mantle structure beneath the Ross Sea Embayment and Marie Byrd Land, West Antarctica, revealed by P-wave tomography, *Earth Planet. Sci. Lett.*, **513**, 40–50, doi:10.1016/j.epsl.2019.02.013.

Yang, Y. & Forsyth, D. W., 2006. Regional tomographic inversion of the amplitude

812 and phase of Rayleigh waves with 2-D sensitivity kernels, *Geophys. J. Int.*, **166**,
813 1148–1160.

Figures

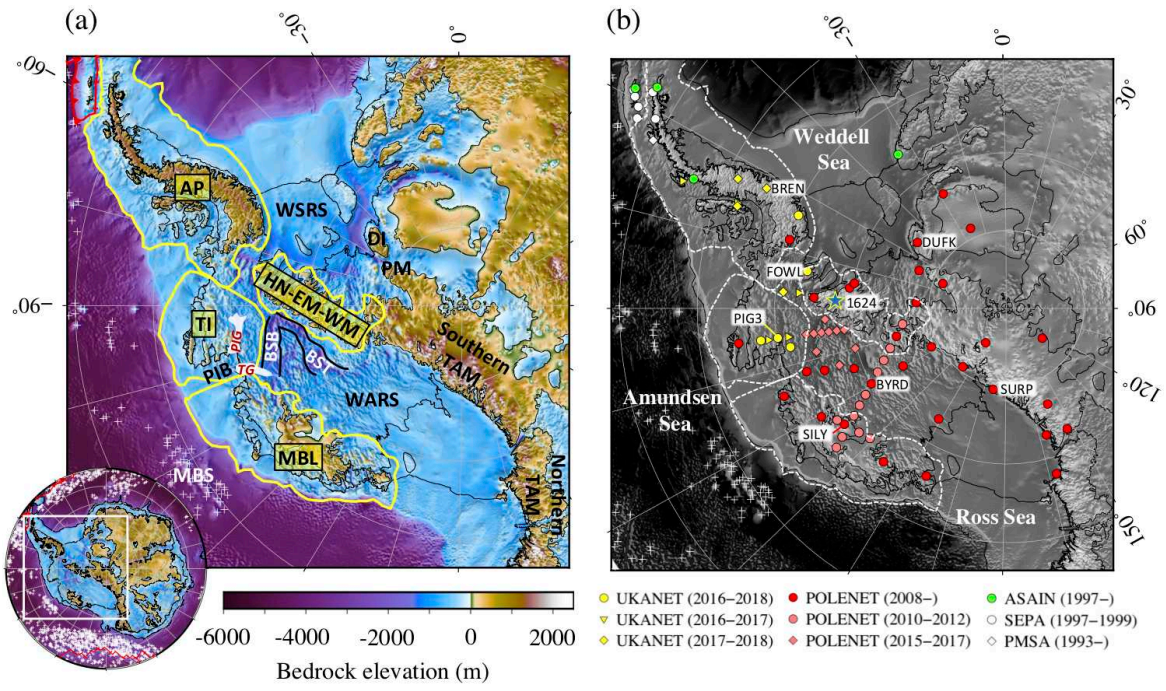

Figure 1: (a) Map of West Antarctic BEDMAP2 bedrock topography (Fretwell et al., 2013). Following Dalziel & Elliot (1982), yellow lines delineate the major crustal blocks of West Antarctica that pre-date Gondwana fragmentation (AP, Antarctic Peninsula; TI, Thurston Island; MBL, Marie Byrd Land; HN-EM-WM, Haag Nunataks-Ellsworth Whitmore Mountains Block, hereafter HEW). The approximate locations of Pine Island Glacier (PIG) and Thwaites Glacier (TG) in the Amundsen Sea Embayment are outlined in white. Plate boundaries are marked in red and white crosses show the locations of seamounts. Other abbreviated geographic features: BSB, Byrd Subglacial Basin; BST, Bentley Subglacial Trench; DI, Dufek Intrusion; MBS, Marie Byrd Seamounts; PIB, Pine Island Bay; PM, Pensacola Mountains; TAM, Transantarctic Mountains; WARS, West Antarctic Rift System; WSRS, Weddell Sea Rift System. (b) Map showing the location of the UKANET, POLENET-ANET, ASAIN, SEPA and GSN seismic stations used in this study superimposed on grey-scale bedrock topography. At initial deployment in January-February 2016, five UKANET seismic stations were arranged in a quasi-linear array straddling Pine Island Glacier, two stations were located approximately north of the HEW block, and three stations were deployed along the southern Antarctica Peninsula. At the end of the first year of the deployment the UKANET array was re-configured to bolster coverage along the southern Antarctic Peninsula. The UKANET seismic array was demobilised in January-February 2018. Specific stations and grid nodes (blue star) referred to in the text are labelled. For interpretation of the references to colour in this figure, the reader is referred to the web version of the article.

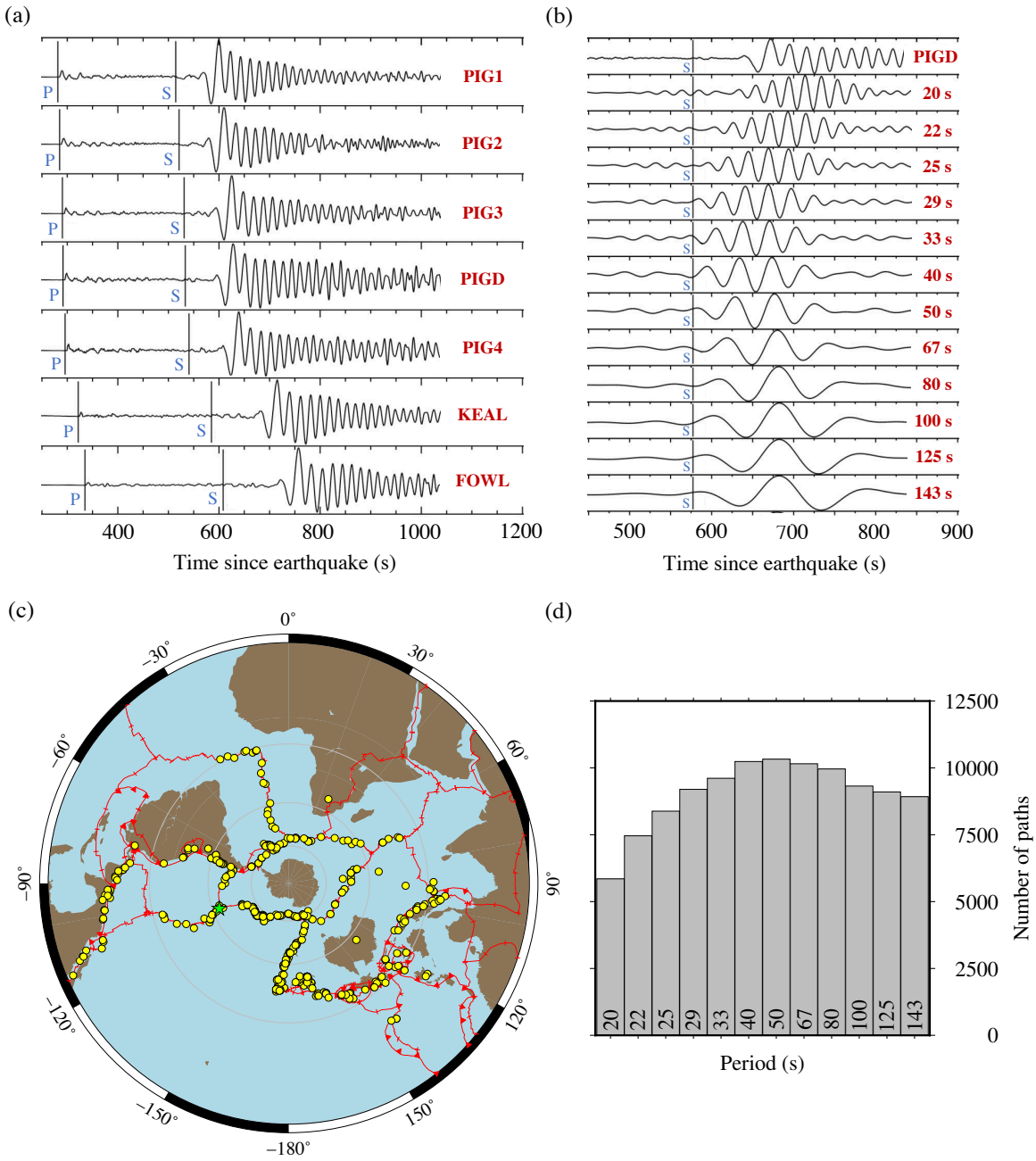

Figure 2: (a) Vertical-component seismograms from a magnitude 6.0 East Pacific Rise earthquake that occurred on August 18^{th} 2016 (green star in (c)) recorded at seven UKANET seismic stations in West Antarctica (see Table S1). Predicted arrival times of compressional (P) and shear (S) body waves according to the Preliminary Reference Earth Model (PREM; Dziewonski & Anderson, 1981) are marked, after which follows the larger amplitude Rayleigh wave. (b) Rayleigh wave dispersion of the same earthquake at UKANET station PIGD. The raw Rayleigh wave seismogram (top) is filtered into 12 × 10 mHz wide frequency bands with centre periods ranging from 20 to 143 s. (c) Azimuthal and epicentral distance distribution of the 457 earthquakes used in this study. Tomographic resolution is enhanced by a uniform azimuthal distribution of earthquakes. Concentric circles are at 30° intervals from the south pole. (d) Total number of ray paths used at each period in this study.

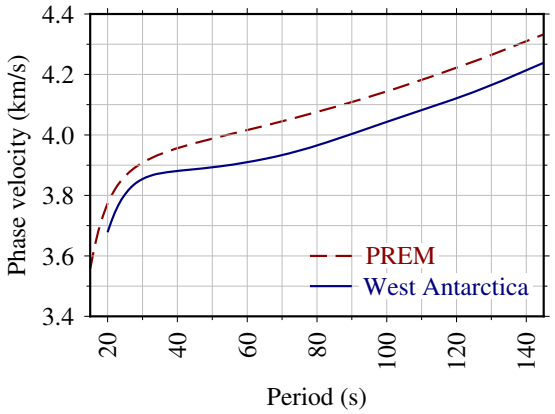

Figure 3: Average Rayleigh wave phase velocity dispersion curve for West Antarctica compared with PREM. The 1D average dispersion curve served as a starting model for subsequent 2D tomographic phase velocity inversions.

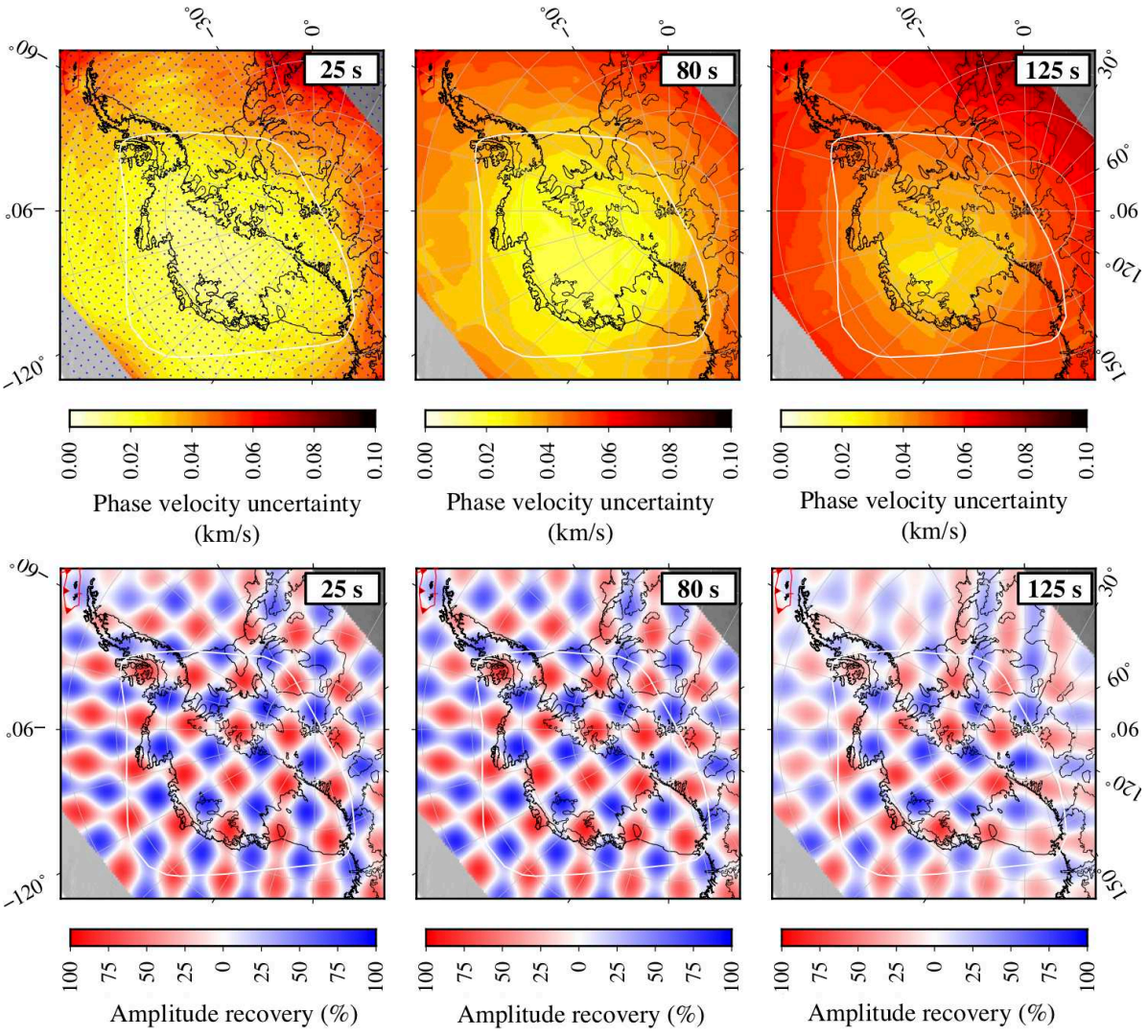

Figure 4: (Top) Rayleigh wave phase velocity model uncertainty at periods 25, 80 and 125 s. Grid node locations are superimposed on the 25 s map. (Bottom) Rayleigh wave phase velocity model resolution at corresponding periods. For ease of visualization, we present the resolution matrix multiplied by a checkerboard pattern of phase velocity anomalies of wavelength 400 km. 100% represents complete amplitude recovery of positive/negative velocity anomalies. We confine our subsequent discussion of imaged structure to the region enclosed by the white polygon.

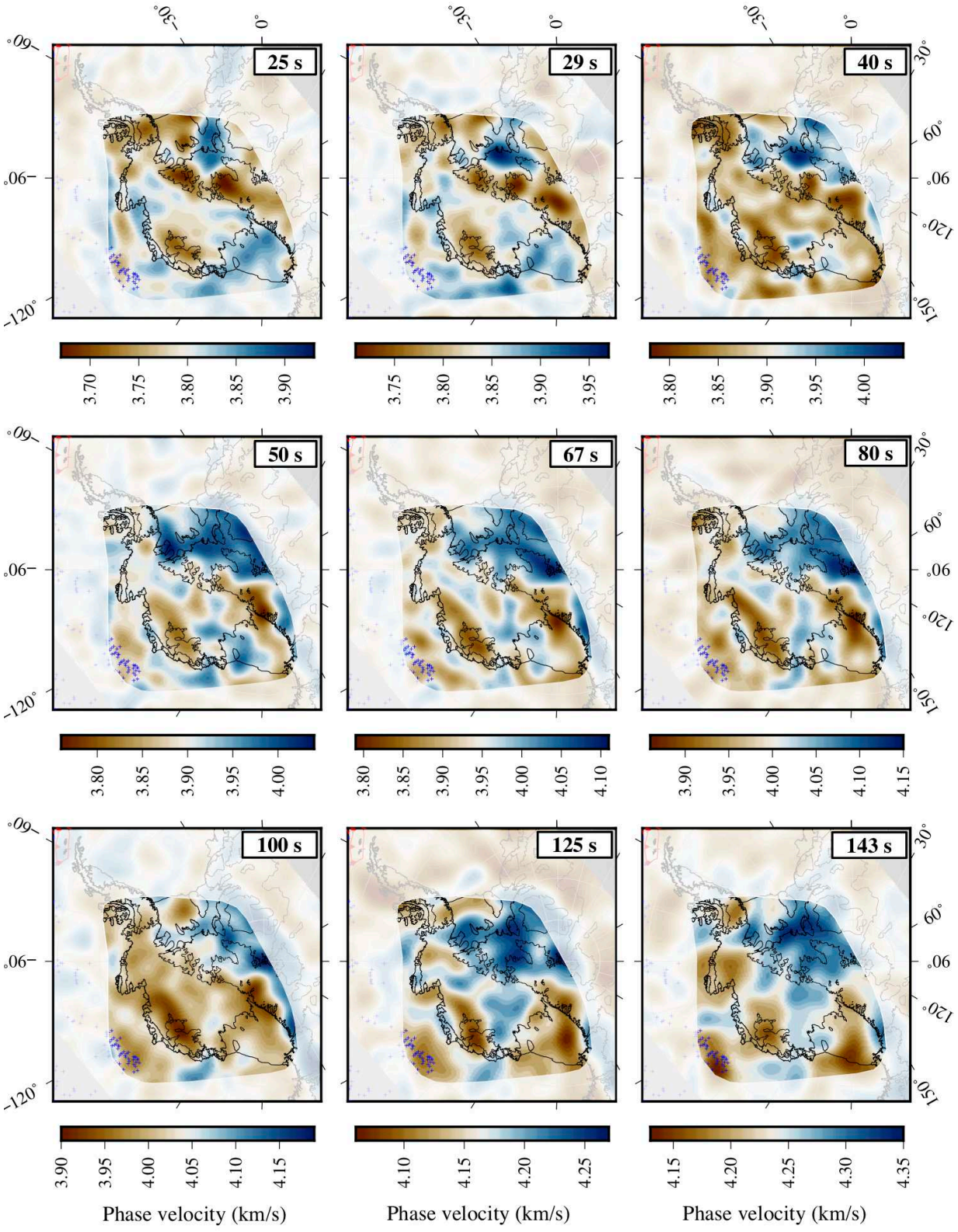

Figure 5: Rayleigh wave phase velocity model at a range of periods. Unique scale bars are used at each period to emphasise lateral velocity variations. Blue crosses show the locations of seamounts. Regions of higher uncertainty and lower resolution are masked.

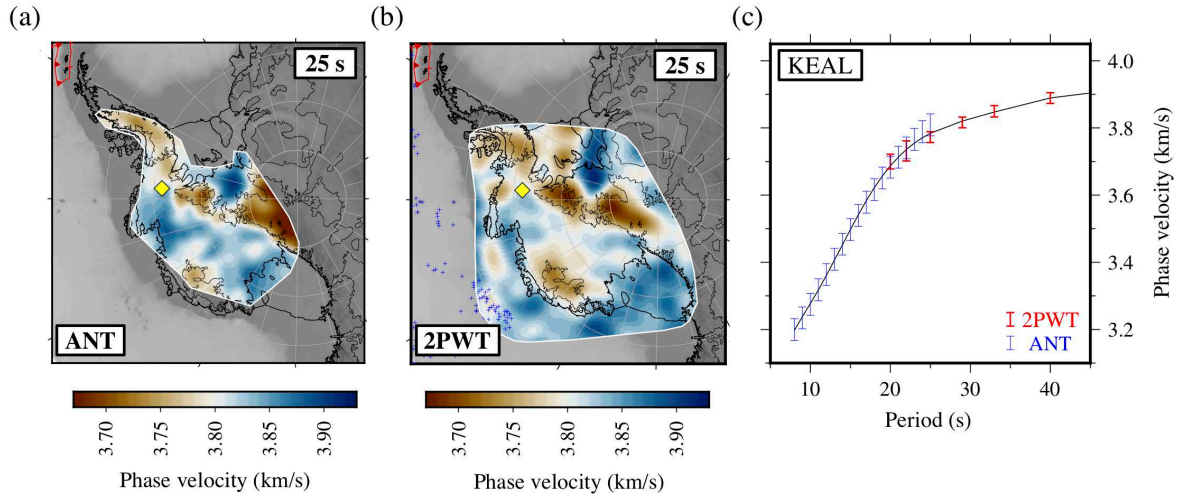

Figure 6: Comparison of Rayleigh wave phase velocity maps at period 25 s inferred by (a) ambient noise tomography (ANT; period range 8-25 s) and (b) two-plane-wave tomography (2PWT; period range 20-143 s). (c) Composite 8-143 s Rayleigh wave phase velocity dispersion curve for UKANET station KEAL obtained by weighted least squares polynomial regression (black curve) of ANT- and 2PWT-curves. The yellow diamond in (a) and (b) shows the location of KEAL.

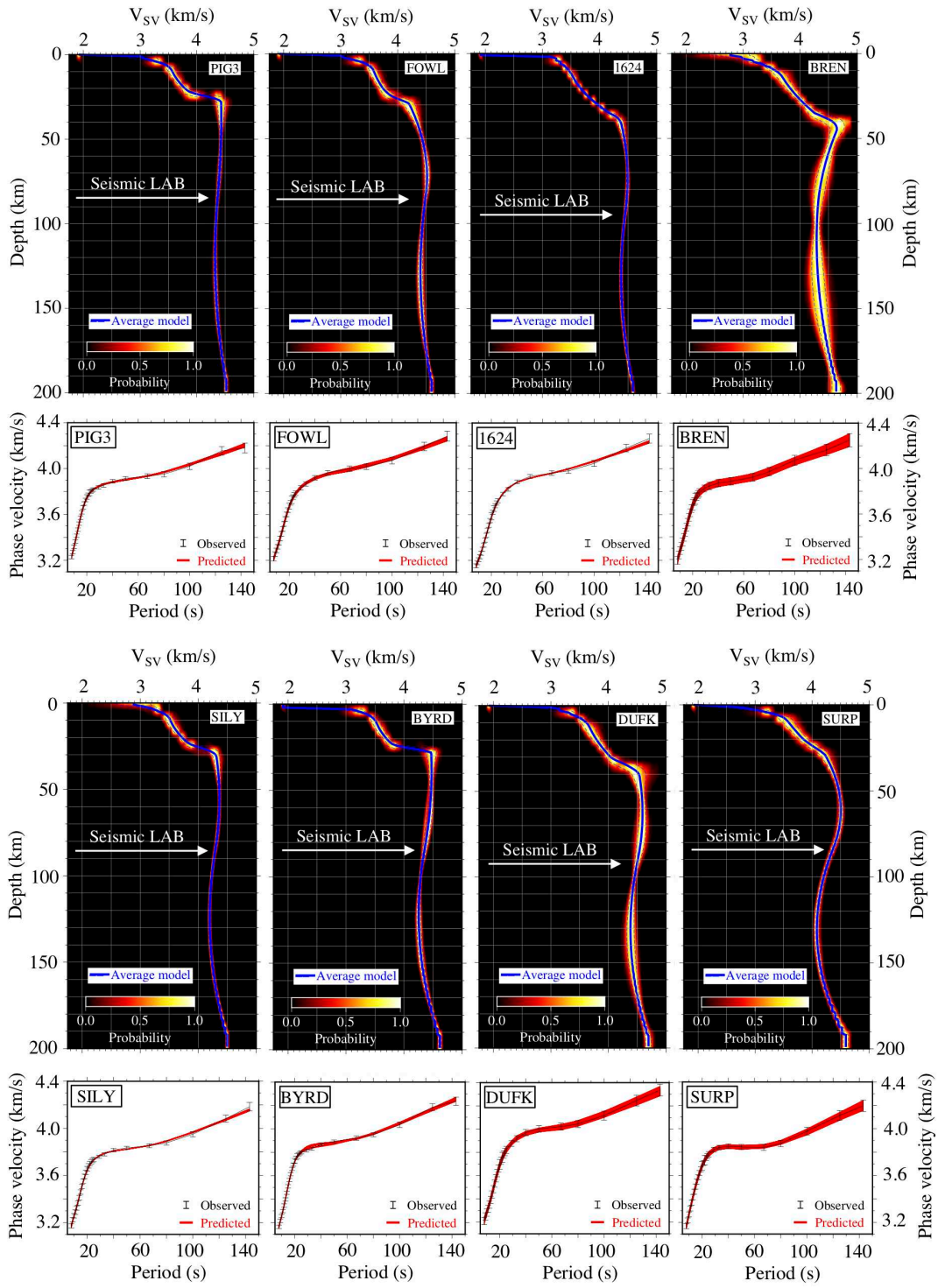

Figure 7: Vertically-polarised shear wave velocity (V_{SV}) profiles inferred from corresponding Rayleigh wave phase velocity dispersion curves. The thick blue line is the mean V_{SV} velocity, the blue dashed lines are one standard deviation bounds. 0 km depth corresponds to the local elevation of the ice sheet surface at each location. The seismic lithosphere-asthenosphere boundary (LAB) is defined here as the depth of the strongest negative velocity gradient at the base of the high velocity seismic lid.

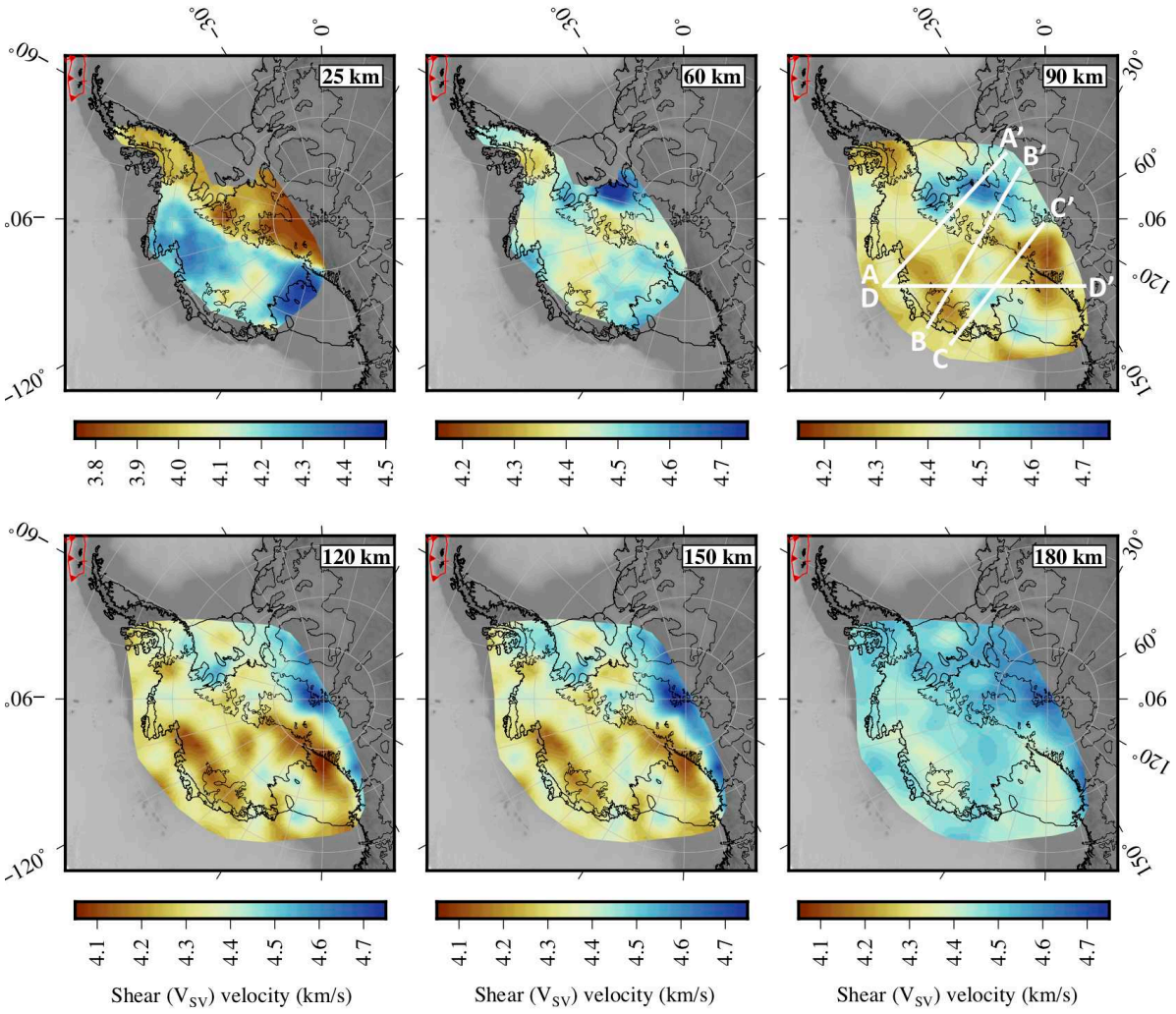

Figure 8: Shear wave velocity (V_{SV}) maps at a selection of depths. We only interpret shallow (<60 km depth) shear wave structure within the footprint of the ANT model. The ANT model domain is more confined than the 2PWT domain, reflected in the varying areal extent of the maps. Shifting scale bars are used to emphasise lateral velocity variations. The locations of the vertical V_{SV} cross-sections shown in Figure 9 are superimposed on the 90 km depth map.

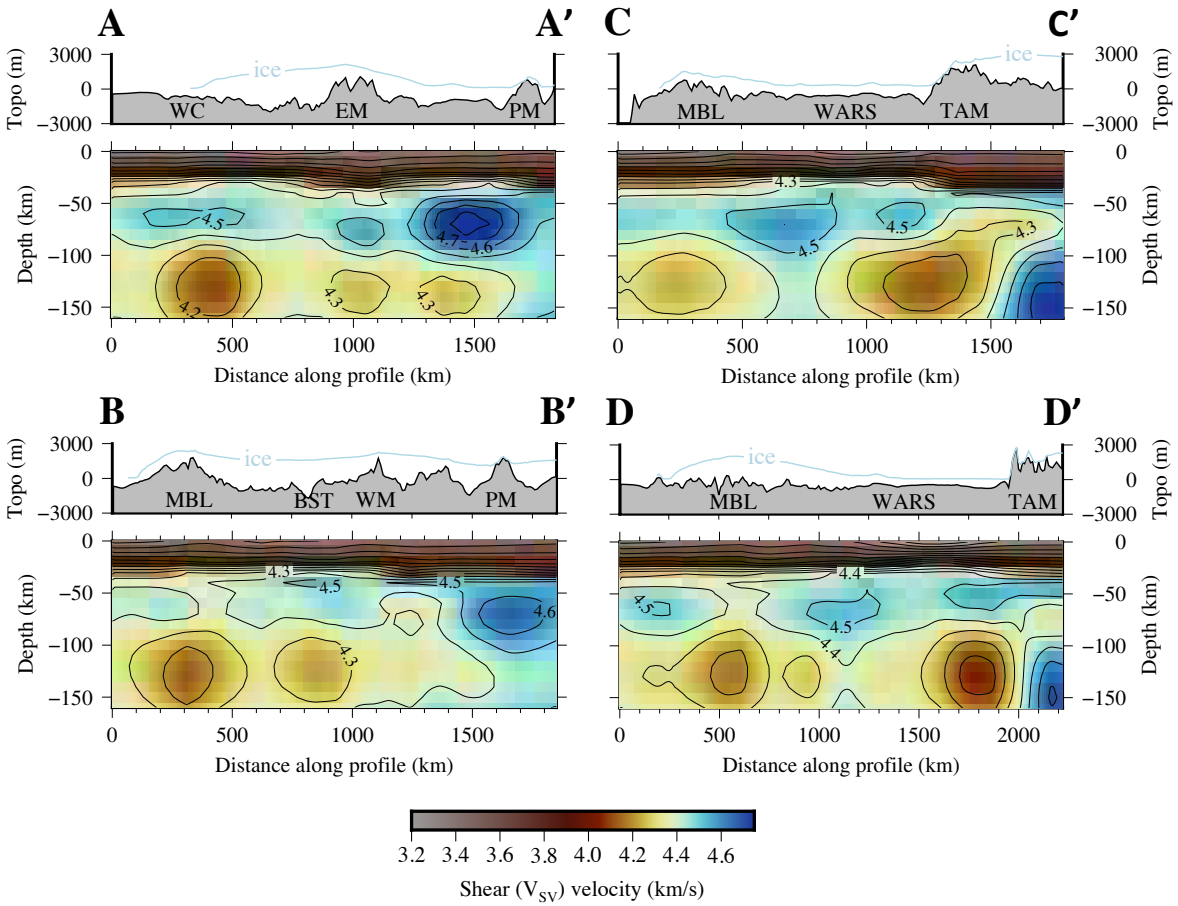

Figure 9: Vertical shear wave velocity (V_{SV}) cross-sections along the four profiles located in Figure 8. The V_{SV} velocities are contoured at 0.1 km/s intervals. Corresponding BEDMAP2 ice and bedrock topography (Topo) profiles are shown in each case. BST, Bentley Subglacial Trench; EM, Ellsworth Mountains; MBL; Marie Byrd Land; PM, Pensacola Mountains; TAM, Transantarctic Mountains; WARS, West Antarctic Rift System; WC, Walgreen Coast; WM, Whitmore Mountains.

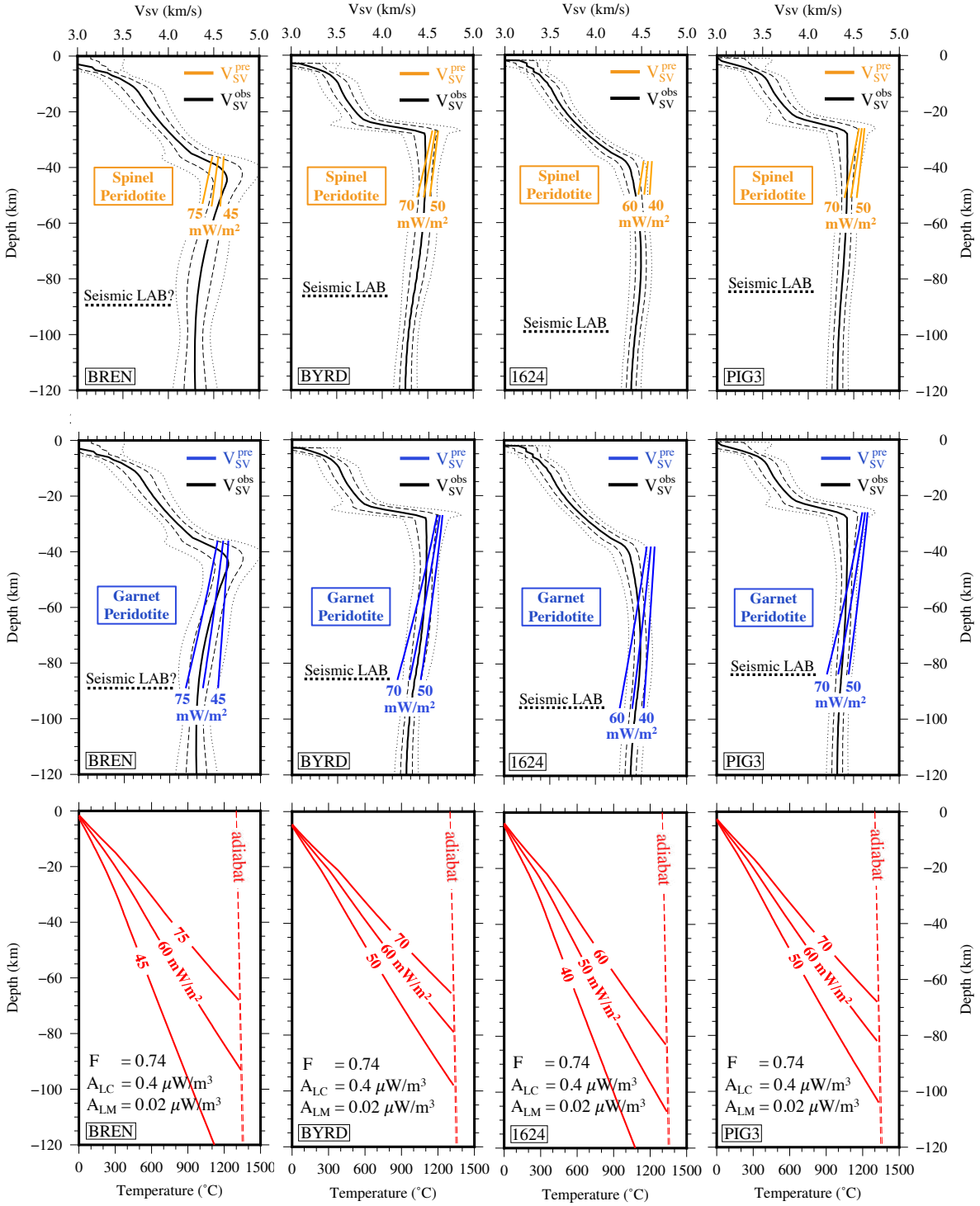

Figure 10: Observed and predicted V_{SV} velocities at seismic stations BREN (southern Antarctic Peninsula), BYRD (central WARS), PIG3 (adjacent to Pine Island Glacier in the Thurston Island block) and node 1624 (Ellsworth Mountains in the HEW block) for spinel peridotite (top) and garnet peridotite lithospheric mantle compositions (middle) corresponding to the steady-state conductive geotherms shown on the bottom. The continuous black V_{SV} profiles represent mean velocities, with dashed and dotted black lines representing one- and two-standard deviation bounds, respectively. Predicted velocity profiles and corresponding geotherms are labelled according to the surface heat flow.